RESEARCH ARTICLE
SPACE PHYSICS: IONOSPHERIC PHYSICS

Earth and Planetary Physics
10: 302–314, 2026
doi: 10.26464/epp2026033

Data-driven simulation of storm-enhanced density and tongue of ionization during the May 10–11, 2024, superstorm

XiangYu Niu[1], Jing Liu[1*], JiaoJiao Zhang[2,3], HaoNan Wu[4], JianJun Liu[5], YaQi Jin[6], and ShuHan Li[1]

[1]Shandong Provincial Key Laboratory of Optical Astronomy and Solar-Terrestrial Environment, School of Space Science and Physics, Institute of Space Sciences, Shandong University, Weihai Shandong 264209, China;

[2]Key Laboratory of Solar Activity and Space Weather, National Space Science Center, Chinese Academy of Sciences, Beijing 100190, China;

[3]Siziwang Observatory of Space Weather, National Space Science Center, Chinese Academy of Sciences, Ulanqab, Inner Mongolia 011800, China;

[4]High Altitude Observatory, National Science Foundation (NSF) National Center for Atmospheric Research, Boulder, CO 80301, USA;

[5]Center for Space Physics and Astronomy, Polar Research Institute of China, Shanghai 201209, China;

[6]Department of Physics, University of Oslo, Oslo 0851, Norway

Key Points:

- Assimilated Special Sensor Ultraviolet Spectrographic Imager (SSUSI) auroral inputs and Super Dual Auroral Radar Network (SuperDARN)-derived convection drivers using the Thomas and Shepherd (2018) model (TS18) allow the Thermosphere–Ionosphere–Electrodynamics General Circulation Model (TIEGCM) to realistically reproduce the May 10–11, 2024, superstorm.
- Data-driven simulation successfully captures the rapid formation of storm-enhanced density and tongue of ionization, yielding improved agreement with the Global Navigation Satellite System (GNSS) total electron content (TEC) relative to empirical drivers.
- Above the F_2 peak, fine-scale $E \times B$ uplift and polar-cap transport dominate, whereas below the peak, auroral precipitation and neutral winds control the development of storm-enhanced density and tongue of ionization.

Citation: Niu, X. Y., Liu, J., Zhang, J. J., Wu, H. N., Liu, J. J., Jin, Y. Q., and Li, S. H. (2026). Data-driven simulation of storm-enhanced density and tongue of ionization during the May 10–11, 2024, superstorm. *Earth Planet. Phys.*, *10*(2), 302–314. http://doi.org/10.26464/epp2026033

Abstract: Storm-enhanced density (SED) and the tongue of ionization (TOI) are key ionospheric storm-time structures whose rapid evolution and fine-scale variability remain challenging to capture with conventional empirical high-latitude drivers. In this study, we examine the May 10–11, 2024, superstorm using the Thermosphere–Ionosphere–Electrodynamics General Circulation Model (TIEGCM) with observation-constrained high-latitude forcing. Auroral precipitation parameters (energy flux and mean energy) are assimilated from a Defense Meteorological Satellite Program (DMSP) Special Sensor Ultraviolet Spectrographic Imager (SSUSI) using a multi-resolution Gaussian process (Lattice Kriging) approach, whereas high-latitude convection potentials are derived by assimilating Super Dual Auroral Radar Network (SuperDARN) observations with the Thomas and Shepherd (2018) model (TS18). For comparison, an additional simulation is performed using empirical models for both convection and auroral forcing. The results show that during the main phase of the May 10 storm, the data-driven simulation provides a more realistic depiction of the SED source region than does the empirical model run by capturing its rapid intensification more clearly and reproducing its spatial location and structural features with higher fidelity. These improvements lead to a more accurate representation of its poleward extension into the polar cap that develops into the TOI. Above the ionospheric F_2 peak over the SED source region, SuperDARN-constrained potentials generate stronger and more localized $E \times B$ drifts that dominate plasma uplift and drive its transport into the polar cap, although neutral winds and downward ambipolar diffusion partially offset these effects. Below the F_2 peak, neutral winds and photochemical processes play a major role in shaping the spatial extent and intensity of the SED and TOI. These results highlight the role of observation-constrained high-latitude drivers in representing ionosphere–thermosphere responses during extreme storms and suggest their relevance for improving physical interpretation and model performance.

Keywords: data-driven simulation; storm-enhanced density; tongue of ionization; continuity term analysis

---

First author: X. Y. Niu, 202317798@mail.sdu.edu.cn
Correspondence to: J. Liu, liujing2019@sdu.edu.cn
Received 27 NOV 2025; Accepted 22 JAN 2026.
First Published online 12 FEB 2026.

1. Introduction

During geomagnetic storms, the ionosphere often shows two remarkable large-scale density structures: storm-enhanced density (SED) and the tongue of ionization (TOI). Storm-enhanced density typically appears in the afternoon–dusk sector at midlatitudes to subauroral regions as a high-density plume that extends poleward and across the dayside; the TOI is the continuation of that plume inside the polar cap, forming a narrow band with sharp edges (Foster, 1993; Kelley et al., 2003; Thomas et al., 2013; Dang T et al., 2019). Observations from Global Navigation Satellite System (GNSS) total electron content (TEC), incoherent scatter radars, and the Defense Meteorological Satellite Program (DMSP) Special Sensor Ultraviolet Spectrographic Imager (SSUSI) show that the SED and TOI are often accompanied by strong variabilities and irregularities that degrade navigation and communication (van der Meeren et al., 2014; Cherniak et al., 2015; Cherniak and Zakharenkova, 2016; Zhang KD et al., 2023). Observations also indicate that SED intensifies rapidly in the afternoon–evening sector, expands poleward, and then threads the polar cap along convection pathways; this continuous track matches transport through the convection throat and is widely regarded as the primary source of the TOI (Foster et al., 2007; Heelis et al., 2009; Liu J et al., 2015, 2016, Liu LB and Wan WX, 2020). The May 10–11, 2024, superstorm was exceptionally intense and displayed SED in two hemispheres with long-lived midlatitude density peaks, so we use it as the representative case in this study (Aa et al., 2024a; Jin YQ et al., 2025).

Observations and models have clarified key aspects of the SED and TOI: GNSS TEC maps, incoherent scatter radars, and *in situ* DMSP plasma together document their onset, rapid growth, and interhemispheric differences (Foster and Rideout, 2007; Yuan ZG et al., 2008). Physics-based coupled ionosphere–thermosphere models, such as SAMI3 and the Thermosphere–Ionosphere–Electrodynamics General Circulation Model (TIEGCM), are used to identify the controlling processes (Huba and Drob, 2017; Pokhotelov et al., 2021). Upward $E \times B$ drifts together with equatorward winds lift plasma to altitudes of reduced recombination rate, favoring SED enhancement (Horvath and Lovell, 2010; Foster et al., 2021). The enhanced midlatitude plasma is subsequently carried poleward by large-scale polar cap convection, developing into the TOI that extends across the polar cap into the nightside high latitudes (Foster et al., 2007; Thomas et al., 2013). These results indicate that storm-time electrodynamic forcing organizes the overall SED and TOI morphology, whereas thermospheric responses modulate its amplitude and persistence (Heelis et al., 1982; Burns et al., 1995).

Despite these advances, standard high-latitude drivers in global models often underestimate or smooth out key storm-time structures (Heelis et al., 1982; Lu X et al., 2023). Empirical auroral inputs underestimate energy deposition and carry little mesoscale or small-scale structure compared with SSUSI observations, thereby weakening heating and the modeled TEC response (Newell et al., 2015; Wu HN and Lu X, 2022). Empirical high-latitude convection potentials are also too smooth, often constrained to tidy two-cell patterns with quasi-fixed boundaries, so they suppress sharp gradients and narrow flow channels documented by the Super Dual Auroral Radar Network (SuperDARN) and incoherent scatter radars (Weimer, 2005; Cousins and Shepherd, 2012; Walach et al., 2022). Consequently, empirically driven runs tend to understate plume strength and TOI penetration, and they capture less of the event-time variability.

Data assimilation mitigates these gaps by blending observations with empirical models in constructing high-latitude drivers that resemble the real system. A multiresolution Gaussian-process framework (Lattice Kriging [LK]) assimilates SuperDARN and Poker Flat Incoherent Scatter Radar (PFISR) drift measurements to reconstruct vector electric fields. It fuses SSUSI and Time History of Events and Macroscale Interactions during Substorms (THEMIS) All-Sky Imager (ASI) auroral observations to estimate the energy flux and mean energy (Lu X et al., 2023). Assimilated convection potentials and electric fields retain mesoscale arcs and channels, sharpen gradients, and reduce artificial boundary jumps. Compared with the smooth empirical high-latitude potentials, they reproduce the rapid, fine-scale variability observed by SuperDARN (Richmond and Thayer, 2000; Papitashvili and Rich, 2002; Chisham et al., 2007). In parallel, the auroral energy inputs are magnified toward observed levels, improving the specification of precipitating energy in space and time (Frey et al., 2004).

We drive the TIEGCM with high-latitude inputs constrained by observations: auroral energy flux and mean energy from SSUSI via multiresolution Gaussian-process assimilation and convection potentials from SuperDARN spherical-harmonic-fit maps. For comparison, we also perform a reference run with conventional empirical drivers. We analyze the May 10–11, 2024, storm as a representative event, using SED and TOI structures as entry points and suggesting a data-assimilation approach guided by observations. When the driver amplitude, update cadence, and mesoscale content are anchored to observations, the assimilation markedly improves model fidelity and applicability during a superstorm. It provides clear direction for forecasting and researching electrodynamic processes.

2. Data and Model Descriptions

2.1 DMSP SSUSI Data and the Assimilation Method

The auroral energy flux and mean energy are derived from the SSUSI instruments onboard the DMSP satellites (Paxton et al., 1992; Paxton and Meng CI, 1999). The SSUSI provides global auroral observations with 0.15° spatial resolution and a 90 min revisit, and the retrieved products have been widely used to specify precipitation drivers in ionosphere–thermosphere models (e.g., Wu HN et al., 2020).

To construct temporally continuous and spatially complete auroral maps, SSUSI observations within ±10 mins of each target Universal Time (UT) are first binned to form instantaneous swaths. To mitigate data gaps between successive satellite passes, additional measurements within ±1 h are linearly interpolated in time, providing improved coverage across the auroral oval (Wu HN et al., 2022). The original and interpolated data are then weighted according to their fidelity—direct SSUSI measurements retain full weight. In contrast, interpolated data are down-sampled to one-third of the native grid density to avoid overrepresentation. This preprocessing ensures that regions covered by actual observations dominate the subsequent assimilation.

The preprocessed SSUSI data are assimilated using the LK model, a multiresolution Gaussian process framework for spatial analysis

(Nychka et al., 2015). The LK model uses nested compact radial basis functions to capture both large-scale patterns and mesoscale auroral structures. It combines all available SSUSI inputs to produce continuous global maps of auroral energy flux and mean energy while preserving mesoscale (10–100 km) variability. To reduce the smoothing artifacts inherent in Gaussian-process fitting, a K-Nearest Neighbor (KNN) postprocessing filter is applied. This step removes nonphysical low-flux values in the polar cap. It sharpens the auroral boundaries, resulting in more realistic high-latitude energy-flux distributions used as time-dependent inputs for the TIEGCM simulation.

2.2 SuperDARN Electric Potentials and Assimilation with the TS18 Model

Large-scale ionospheric convection is specified using SuperDARN line-of-sight velocity measurements, which are combined into global convection maps (Ruohoniemi and Greenwald, 1998; Shepherd and Ruohoniemi, 2000). As of 2024, SuperDARN consisted of 39 radars, including six newly built Chinese stations (CN-DARN) at Longjing, Siziwang, and Hejing, which greatly expand coverage across Asia and enable unprecedented storm-time convection observations (Nishitani et al., 2019; Zhang JJ et al., 2024).

SuperDARN data are assimilated with the TS18 empirical model (Thomas and Shepherd, 2018) to obtain continuous high-latitude potentials, thereby compensating for gaps in SuperDARN observations. The assimilation follows the SuperDARN Assimilative Mapping (SAM) framework (Cousins et al., 2013), in which radar line-of-sight velocities are fitted together with the TS18 background potential by using a weighted least-squares approach. Measurement uncertainties determine observation weights, whereas the background model provides global constraints in regions without radar echoes. The resulting convection potentials preserve the large-scale two-cell structure while incorporating SuperDARN-observed mesoscale features, offering realistic electrodynamic drivers for the TIEGCM simulation.

2.3 TIEGCM Description and Term Analysis Method

The TIEGCM (version 2.0) is a time-dependent, three-dimensional global model that self-consistently simulates key thermospheric and ionospheric processes, including neutral composition, temperature, winds, ionospheric transport, electric fields, and current systems (Roble et al., 1988; Richmond et al., 1992; Qian LY et al., 2014). In this study, the model is configured with a horizontal resolution of 2.5° × 2.5° and 60 pressure levels spanning altitudes from approximately 97 to 500 km. At the lower boundary, migrating and nonmigrating tides originating from the lower atmosphere are specified using the Global Scale Wave Model, whereas all other boundary conditions follow the standard TIEGCM configuration.

Two sets of simulations are performed in this study. In the reference simulation, high-latitude electrodynamic forcing is specified using the Weimer empirical electric potential model together with empirical auroral particle precipitation (Roble and Ridley, 1988; Weimer, 2005). In the data-driven simulation, the high-latitude forcing is replaced by observation-constrained inputs, in which convection potentials derived from SuperDARN observations and auroral precipitation parameters obtained from DMSP SSUSI measurements are assimilated and used as external drivers for the TIEGCM. This experimental design allows a direct comparison between empirical and observation-constrained high-latitude forcing during the storm period.

To investigate the evolution of SED and its polar-cap extension as the TOI, we apply a term analysis of the ion continuity equation in the vicinity of the F_2 peak. This diagnostic framework has also been used in previous studies to separate the relative contributions of different physical processes to ionospheric density variations (Lei JH et al., 2008). The O^+ continuity equation can be written as

$$\frac{\partial N_{O^+}}{\partial t} = q_{O^+} - \beta N_{O^+} - \nabla \cdot (N_{O^+}\boldsymbol{V}), \tag{1}$$

where N_{O^+} is the O^+ density, q_{O^+} is the production rate, β is the effective loss coefficient, and $\boldsymbol{V}$ is the ion velocity. The first two terms on the right-hand side represent chemical production and loss, whereas the last term denotes plasma transport. The transport term can be further separated into contributions from neutral wind transport, $E \times B$ drift, and ambipolar diffusion.

In the F_2 region, O^+ is the dominant ion, so the electron density can be approximated by the O^+ density (Rishbeth and Garriott, 1969). Because their density variations are numerically similar, the continuity equation can be written in terms of electron density and decomposed into contributions from chemical ($\delta NE_{\rm ch}$), neutral wind ($\delta NE_{\rm w}$), $E \times B$ ($\delta NE_{E\times B}$), and ambipolar diffusion terms ($\delta NE_{\rm Ambi\_diff}$):

$$\delta NE = \delta NE_{\rm ch} + \delta NE_{\rm w} + \delta NE_{E\times B} + \delta NE_{\rm Ambi\_diff}. \tag{2}$$

3. Results

Figure 1 shows the interplanetary and geomagnetic conditions on May 10, 2024, at 16:00–24:00 UT. After commencement of the sudden storm at ~17:00 UT, interplanetary magnetic field (IMF) B_z turned southward following 18:00 UT and remained mostly between −20 and −30 nT, reaching more negative values near 20:00 UT. Interplanetary magnetic field B_y was highly variable, with a sharp reversal between 22:20 and 22:40 UT from negative to positive values exceeding 80 nT. During this interval, the solar wind speed remained above 700 km/s, and the dynamic pressure showed pronounced fluctuations. The geomagnetic response was intense: SYM-*H* decreased rapidly to approximately −300 nT, marking the development of the storm main phase. The *AE* index increased to more than 2000 nT with repeated intensifications, demonstrating strong substorm activity.

Given the storm-time geomagnetic indices in Figure 1, realistic high-latitude inputs are required for the model; Figure 2 provides the energy flux and electric potential from observations, empirical models, and the assimilation. Figure 2a shows the auroral energy flux from DMSP SSUSI at 19:00 UT, with intense precipitation in the evening sector (~16–21 magnetic local time [MLT], 60°–70° magnetic latitude [MLAT]) and additional enhancements on the dawn side (~4–9 MLT); the spatial coverage is restricted to the satellite pass. Figure 2b presents the empirical specification based on the Zhang Y and Paxton (2008) model, which reproduces the

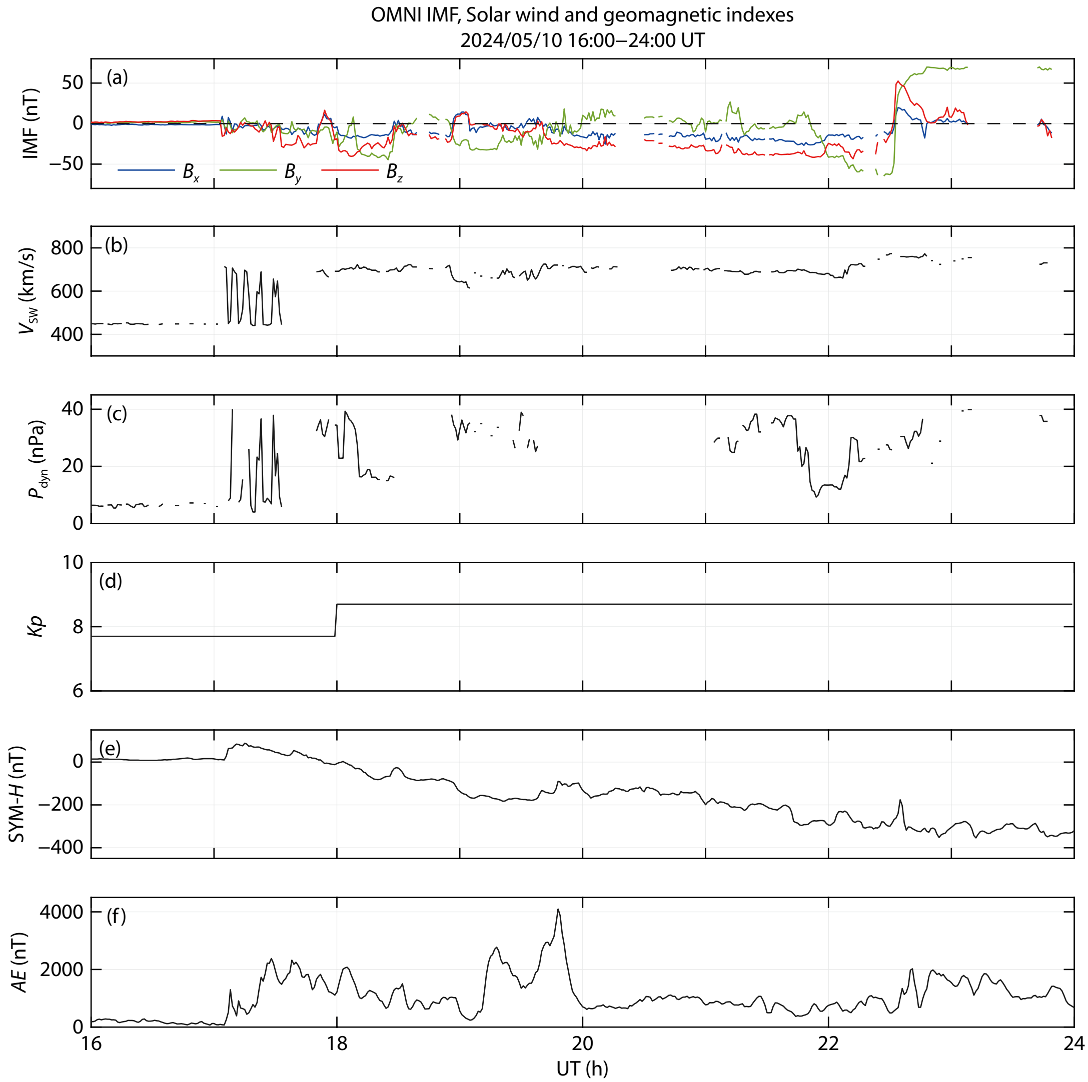

Figure 1. Solar wind and geomagnetic conditions on May 10, 2024, from 16:00 to 24:00 UT. (a) Interplanetary magnetic field (IMF) components B_x (blue), B_y (green), and B_z (red) in GSM (Geocentric Solar Magnetospheric) coordinates. (b) Solar wind speed (V_{SW}). (c) Dynamic pressure (P_{dyn}). (d) *Kp* index. (e) SYM-*H* index. (f) *AE* (auroral electrojet) index.

large-scale oval morphology but appears overly smooth and systematically underestimates the flux magnitude relative to observations. Figure 2c gives the assimilation result obtained by combining SSUSI with the empirical background through a multiresolution Gaussian process, which captures mesoscale structures revealed by the observations while providing full polar coverage. This comparison shows that assimilation combines observations and empirical models to yield a more realistic input specification.

Figure 2d shows SuperDARN line-of-sight velocities at 19:00 UT, with radar backscatter mainly in the noon–afternoon (~12–18 MLT) and midnight–dawn (~0–6 MLT) sectors. The measurements reveal localized convection signatures, but the spatial coverage remains limited. Figure 2e presents the Weimer empirical potential, which reproduces the large-scale two-cell convection but is overly smooth. Figure 2f shows the spherical-harmonic-fit potential derived from assimilating the radar velocities, which retains sharper gradients and localized variations consistent with the measurements while maintaining full polar coverage. The comparison between Figures 2e and 2f demonstrates that the spherical-harmonic-fit solution constrained by observations reduces the excessive smoothing of the empirical model and better represents the spatial details of the convection pattern.

Figure 2 shows that assimilation yields energy, energy flux, and electric potential fields that are broadly consistent with observations and provide full spatial coverage. These assimilated maps are used as external drivers for the data-driven TIEGCM.

Figure 3 shows the storm-time TEC difference on May 10, 2024, relative to the quiet day of May 9, 2024, corresponding to the main phase interval from 17:00 to 22:00 UT. This figure illustrates the evolution of the storm-time TEC response on May 10, 2024, from initial regional increases to plume-like SED signatures and subsequent poleward extensions observed in both hemispheres. At 17:00–18:00 UT, the response is still weak, with only small positive values over the American sector. By 19:00 UT, a clear enhance-

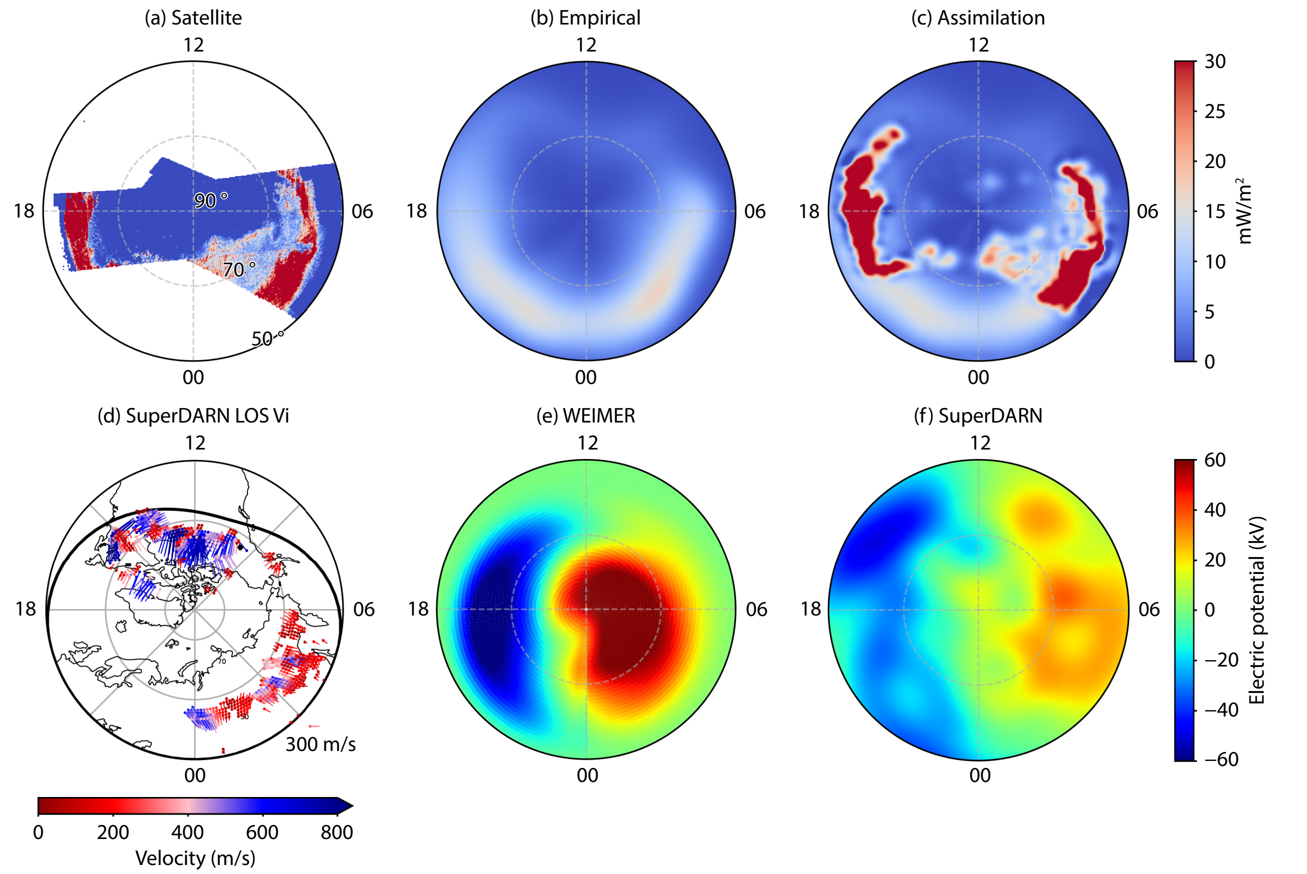

Figure 2. Auroral energy flux and high-latitude potential from different sources. (a) Auroral energy flux from DMSP SSUSI observations, (b) the empirical model, and (c) the assimilated energy flux constrained by SSUSI observations. (d) SuperDARN radar line-of-sight (LOS) velocities, (e) Weimer empirical potential, and (f) assimilated electric potential derived from SuperDARN observations by using the TS18 scheme. The assimilated flux (c) and electric potential (f) are used as external inputs to drive the data-driven TIEGCM simulation.

ment appears over South America and the adjacent Atlantic in the evening sector, showing a plume-like feature extending poleward. Consequently, in the northern hemisphere, the American longitude sector around 18:00–22:00 UT represents the optimal location and timing for SED development, as supported by numerous case studies and statistical analyses (Foster et al., 2021; Aa et al., 2024b).

At 20:00–21:00 UT, the positive storm effects intensify and expand, forming a well-defined plume from midlatitudes to higher latitudes. The structure broadens in both latitude and longitude, indicating a strong storm-time redistribution of plasma (Du JH and Yang Z, 2025). At the same time, a negative ΔTEC is observed in Canada north of the United States. Similar regional enhancements and poleward extensions have also been described during other storms (Liu J et al., 2016).

By 22:00 UT, a strong positive ΔTEC persists in both hemispheres over the American sector, with elongated structures extending deep into the polar regions. The contrast between the significant enhancement in the dusk–midnight sector and negative responses elsewhere indicates pronounced spatial variability. Aa et al. (2024a) likewise reported strong SED and TOI features over this sector at 20:30–22:30 UT.

Figure 4 presents the evolution of TEC differences in MLAT–MLT coordinates from 18:00 to 22:00 UT on May 10, 2024, with convection electric potentials superposed. The left column shows GPS-derived TEC differences with SuperDARN potentials, the middle column shows data-driven TIEGCM TEC differences with assimilated electric potentials, and the right column shows Weimer-driven TIEGCM TEC differences with empirical potentials.

At 18:00 UT, all three northern hemisphere maps show only weak responses. By 19:00 UT, the GPS observations display a plume-like enhancement in the evening sector over the American longitude, extending poleward along the convection channels indicated by SuperDARN, a typical signature of TOI formation. The data-driven TIEGCM reproduces both the plume structure and its poleward extension in close agreement with the observations. In contrast, the Weimer-driven simulation shows a broad, large-scale increase but lacks a well-defined plume, and the associated TOI does not extend distinctly into the polar cap.

At 20:00–21:00 UT, the GPS TEC maps show that the plume intensifies and extends further into the polar cap, with the enhancement aligned with the cross-polar flow and the return flow in the dusk sector indicated by the SuperDARN potentials. This morphology is characteristic of a well-developed TOI (Kelley et al., 2004; Foster and Rideout, 2007; Liu J et al., 2015). The data-driven TIEGCM

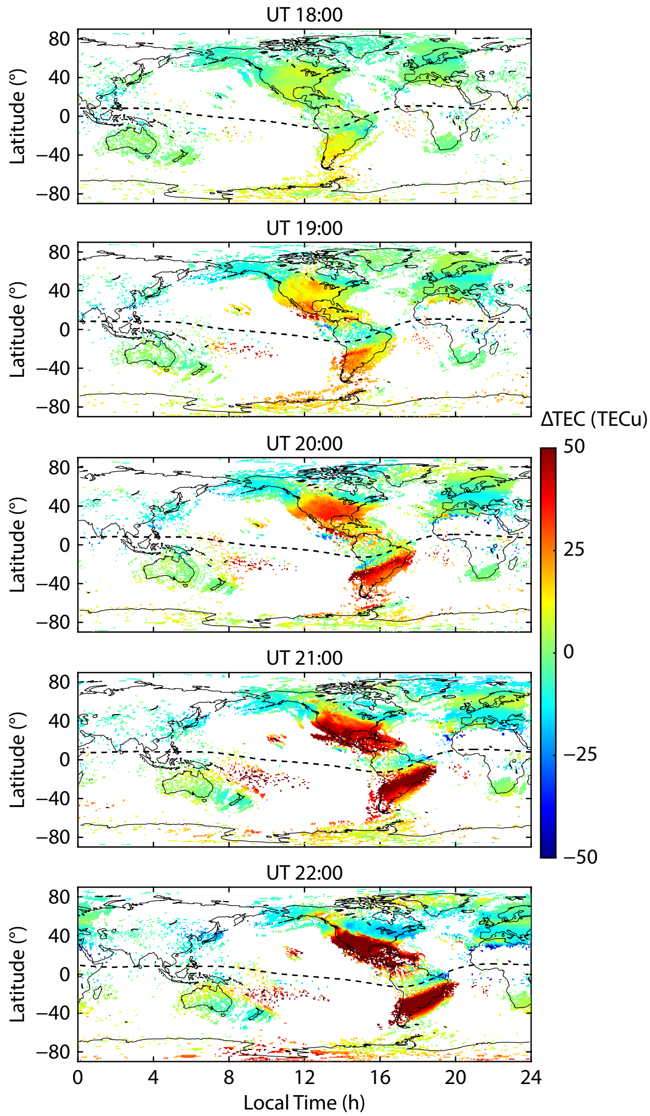

Figure 3. Global distributions of ΔTEC on May 10, 2024, relative to May 9, 2024, shown hourly from 17:00 to 22:00 UT.

reproduces both the amplitude and spatial structure more realistically; in addition, it captures electron density increases within the auroral oval that are consistent with the observations. Some local overestimation is evident along the TOI region, but the spatial progression and alignment with the convection streamlines remain in close agreement with the measurements. In contrast, the Weimer-driven simulation maintains a reasonable two-cell convection configuration, but the associated TEC and potential patterns are broader and smoother (Wu HN and Lu X, 2022). Therefore, the plume penetration into the polar cap is weaker, and mesoscale details are less evident compared with the observations and assimilation results.

By 22:00 UT, the plume undergoes further development, extending to higher latitudes with the TOI extending poleward of the auroral oval and penetrating the polar cap. The data-driven TIEGCM reproduces this deeper latitudinal extension and its associated potential pattern, indicating that assimilation more effectively maintains TOI evolution consistent with the observations. In contrast, although the Weimer-driven run also shows enhancement in the same sector, its penetration into the polar cap is noticeably weaker, and the structure is more diffuse, making it unable to capture the well-developed TOI morphology evident in the measurements.

Although we have incorporated more realistic electric field and auroral energy drivers into the model to simulate ionospheric changes during storms more accurately, the predictions in the negative storm regions, including TEC depletion areas observed at 21:00 and 22:00 UT, primarily in the nightside high-latitude regions, remain imperfect in both the data-driven and Weimer simulations. During these periods, TEC values in these regions are consistently higher than expected. Because of inherent assumptions and approximations, the TIEGCM has difficulty capturing the rapid changes in thermospheric temperature, density, and gas composition during major geomagnetic storms, leading to deviations in TEC predictions. The existing model is unable to capture these rapid changes accurately, thus affecting model accuracy.

Figure 5 illustrates the differences between storm time and quiet time in the data-driven modeled F_2 layer peak density (N_mF_2), peak height (h_mF_2), ion drifts, and O/N_2 at 19:00 UT on May 10, 2024. A prominent feature is the well-defined two-cell ion convection pattern, with the O/N_2 distribution showing a comparable morphology. Along the noon–midnight meridian, a poleward-extending O/N_2 "tongue" develops, driven by the advection of O/N_2-rich midlatitude air parcels and reinforced by frequent neutral–plasma collisions (Foster, 1993; Burns et al., 2004). In the noon throat region, intense upward ion drifts raise h_mF_2 by approximately 80–120 km, accompanied by enhanced N_mF_2. These storm-time signatures are characteristic of the SED and TOI.

4. Discussion

Figure 6 presents the term analysis results at 19:00 UT on May 10, 2024, illustrating the relative contributions of different physical processes to electron density variations. In the topside ionosphere, the dayside throat is characterized by enhanced electron density perturbations, which identify the source region of SED and its subsequent extension into the polar cap as the TOI. At this altitude, the chemical term (Figure 6, second row) is negligible because the concentrations of O and N_2 are low and recombination is inefficient, thereby exerting only a minimal influence on the overall morphology (Liu J et al., 2016).

Below the ionospheric F_2 peak in the nightside auroral region (60°–75° MLAT), the assimilated drivers enhance the auroral energy deposition prescribed in the model, causing precipitating electrons to deposit more energy between 150 and 300 km and to produce additional ionization through collisions with N_2 and O_2 (Hardy et al., 1987; Fang XH et al., 2008). This results in strengthened electron density perturbations at 280 km on the equatorward side of the auroral oval. In the same latitudinal band, the chemical term (Figure 6, second row) also increases because precipitation-driven ionization enhancement raises the local production rate relative to recombination, yielding a larger net chemical contribution (Solomon et al., 1988). Along the dayside SED channel, the chemical term exhibits a pronounced positive contribution. As

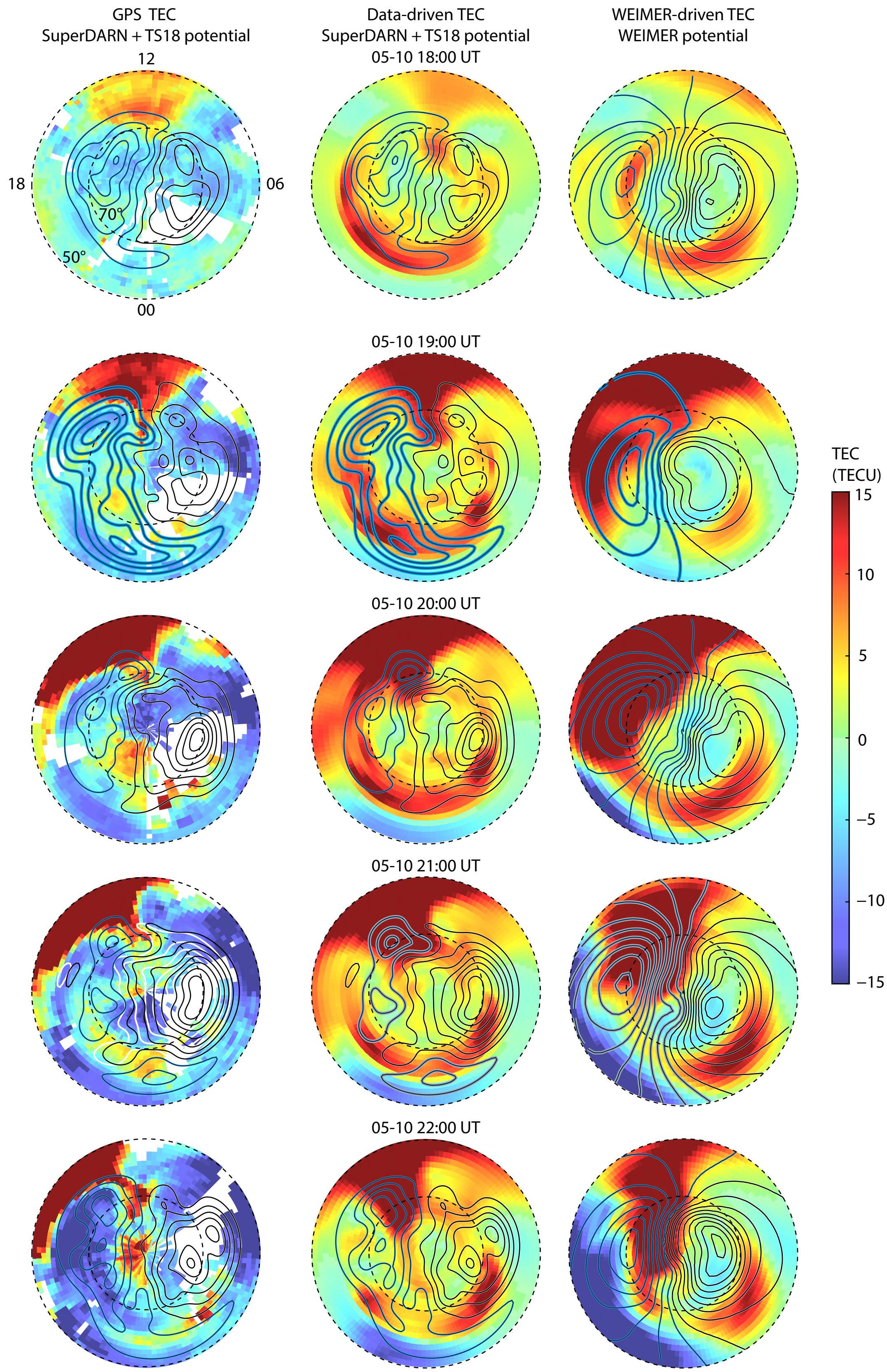

Figure 4. Sequences of TEC difference maps in MLAT (40°–90°) and MLT coordinates from 18:00 to 22:00 UT on May 10, 2024. Convection electric potentials are superposed for different TEC differences: GPS observations with SuperDARN potential (left), data-driven TIEGCM with SuperDARN potential (middle), and Weimer-driven TIEGCM with Weimer potential (right). The equipotential contours are drawn at 6 kV intervals for the GPS and data-driven panels, and 10 kV intervals for the Weimer-driven case.

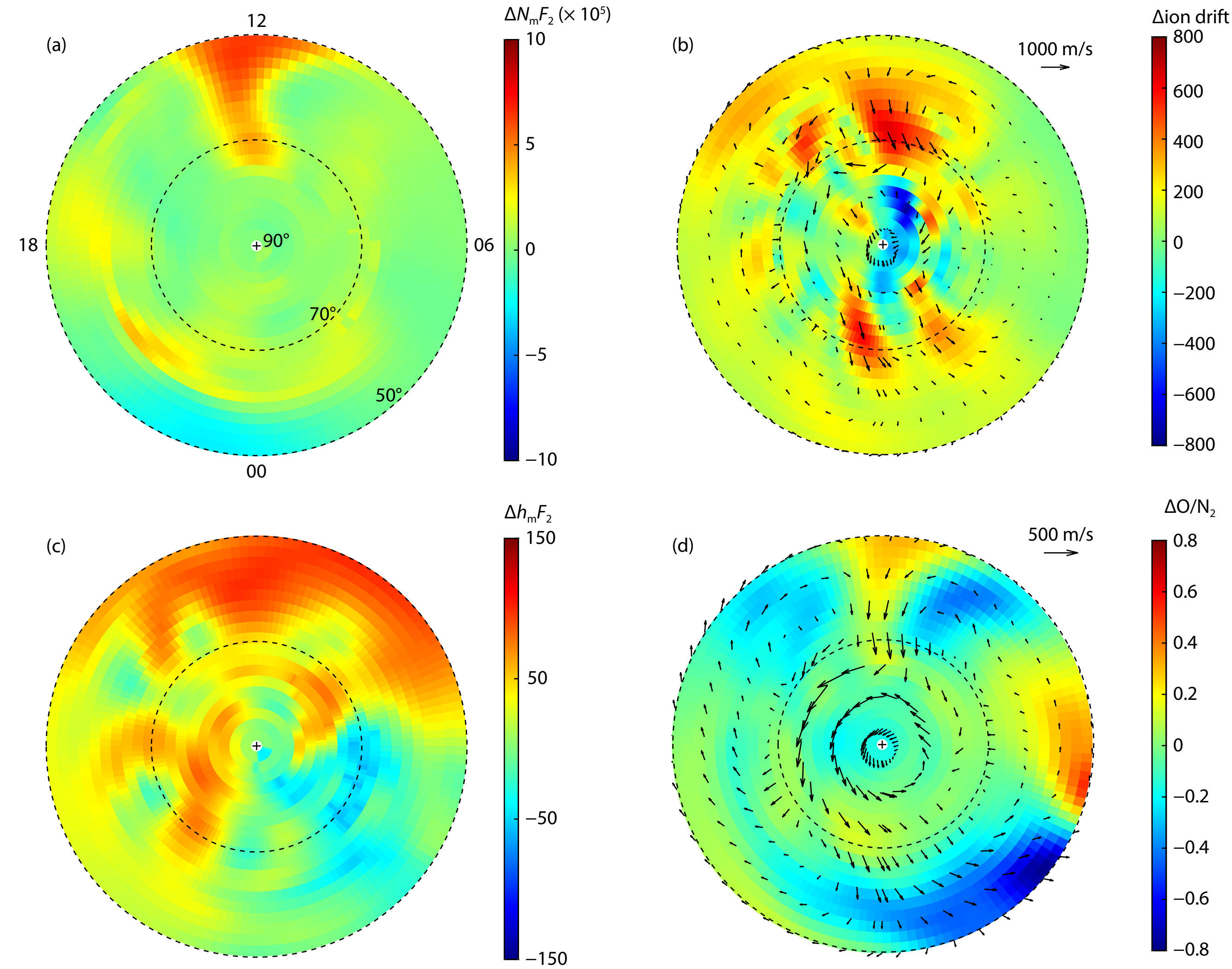

Figure 5. Polar view of the data-driven modeled absolute difference between storm time (May 10) and quiet time (May 9) in N_mF_2, h_mF_2, ion drifts, and O/N_2 at 19:00 UT. The left column shows ΔN_mF_2 and Δh_mF_2. The right column shows Δion drift and $\Delta O/N_2$, with arrows denoting the vector differences in ion drifts and neutral winds, respectively.

illustrated in Figure 5, this channel features enhanced electron density and a pronounced uplift of h_mF_2, placing the plasma at altitudes where photoionization remains effective. At the same time, reduced molecular densities weaken recombination. Under these conditions, chemical production becomes increasingly dominant, consistent with previous findings indicating that an elevated F_2 peak suppresses molecular recombination and strengthens ionospheric production (Torr et al., 1979; Robinson et al., 1987; Tsurutani et al., 2004). As data assimilation improves the spatial representation of the SED structure, the intensified chemical contribution aligns more closely with the observed high-density pathway. It exhibits sharper local variations along its poleward extension toward the TOI.

In the SED and TOI regions, the wind term exhibits distinct altitude-dependent responses. As shown in Figure 6 (third row), the wind contribution becomes negative above the ionospheric F_2 peak, indicating that poleward neutral winds, together with the inclined geomagnetic field, drive plasma downward along magnetic field lines. Below the ionospheric F_2 peak, however, the wind term becomes positive along the SED and TOI pathways, revealing a clear contrast between regions above and below the F_2 peak (Deng and Ridley, 2006).

This vertical contrast can be understood from the neutral-wind transport term in the plasma continuity equation (Liu et al., 2025),

$$\delta N_{\text{wind}} = -\nabla \cdot (N_{O^+} \boldsymbol{V}_{i\_\text{wind}}) = -N_{O^+} \nabla \cdot \boldsymbol{V}_{i\_\text{wind}} - \boldsymbol{V}_{i\_\text{wind}} \nabla N_{O^+}, \quad (3)$$

where $\boldsymbol{V}_{i\_\text{wind}}$ denotes the ion velocity induced by ion–neutral drag and N_{O^+} is the O^+ number density. Near h_mF_2, the wind contribution is dominated by the $-\boldsymbol{V}_{i\_\text{wind}} \nabla N_{O^+}$. Because h_mF_2 corresponds to the altitude of maximum O^+ density, the vertical density gradient is positive below h_mF_2 and negative above h_mF_2. As the neutral wind varies weakly with height near the F_2 peak, the same wind-driven ion motion acts on density gradients of the opposite sign. This leads to a vertical phase reversal of the wind term, with negative contributions above the F_2 peak and positive contributions below the F_2 peak along the SED and TOI pathways.

In this study, the convection potential is constrained by SuperDARN

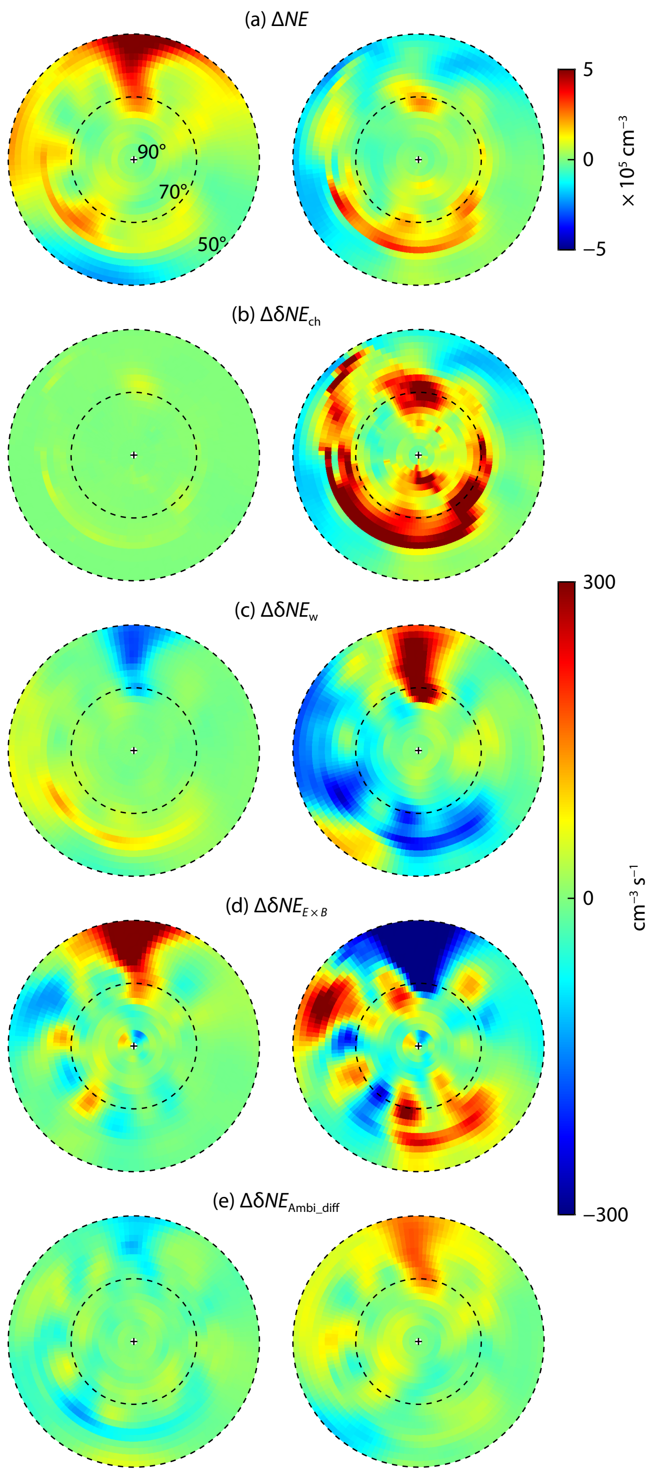

Figure 6. The modeled absolute difference from the data-driven TIEGCM simulation between storm-time (May 10, 2024) and quiet-time (May 9, 2024) electron density (in units of 10^5 cm^{-3}) and the electron density change rate caused by chemical processes ($\Delta\delta NE_{\rm ch}$), neutral wind transport ($\Delta\delta NE_{\rm w}$), electric field transport ($\Delta\delta NE_{E\times B}$), and ambipolar diffusion ($\Delta\delta NE_{\rm Ambi_diff}$) terms (in units of cm^{-3} s^{-1}) at 19:00 UT. The first column denotes the terms at ~500 km (pressure level 3.625), and the second column denotes those at ~280 km (pressure level 1.125).

data, leading to a more accurate representation of the two-cell convection pattern and high-latitude channels. As shown in Figure 6 (fourth row), the upward $E \times B$ drift above the ionospheric F_2 peak lifts plasma to higher altitudes, facilitating the formation of SED and TOI structures. The assimilated drivers capture localized, rapidly changing electric field structures, particularly in high-latitude regions, where fluctuations in the electric field guide plasma propagation. These electrodynamic boundaries more effectively guide plasma into the polar region. The SuperDARN electric potential drive introduces mesoscale and small-scale electric field structures, allowing electron density to follow these evolving boundaries into the polar region, thereby enhancing the transport of SED into the TOI region. Below the F_2 peak, the electric field term weakens, reducing upward drift and limiting plasma transport along the SED and TOI pathways (Deng and Ridley, 2006). The data-driven electric field improves the capture of electric field variations. It enhances plasma transport simulations, especially in the polar region, further improving the ability of the model to reflect plasma dynamics in this region accurately.

Figure 6 (fifth row) shows the contribution of ambipolar diffusion to electron density variations. Its overall magnitude is much weaker than that of the wind and electric field terms, indicating a secondary role during the storm. In the topside ionosphere, ambipolar diffusion tends to reduce electron density, whereas below the ionospheric F_2 peak, it tends to enhance it. This opposite pattern reflects the classical behavior of ambipolar diffusion, in which elevated plasma density and temperature in the topside ionosphere under external heating accelerate downward diffusion, leading to increased density at lower altitudes.

Figure 7 shows the latitude–altitude distributions of the absolute differences in electron density change (ΔNE, first row, in units of 10^5 cm^{-3}) and its individual driving terms (in units of cm^{-3} s^{-1}): production and loss ($\Delta\delta NE_{\rm ch}$, second row), neutral wind transport ($\Delta\delta NE_{\rm w}$, third row), electric field transport ($\Delta\delta NE_{E\times B}$, fourth row), and ambipolar diffusion ($\Delta\delta NE_{\rm Ambi_diff}$, fifth row). The results are obtained from the data-driven TIEGCM simulation, when the SED and TOI structures appear at 12 LT during the main phase of the storm. The electron density enhancement is mainly confined to 45°–60°N latitudes and altitudes between 350 and 600 km. The $\Delta\delta NE_{\rm ch}$ shows positive contributions at 240–400 km, indicating that enhanced ion production outweighs chemical losses in this altitude range. The $\Delta\delta NE_{\rm w}$ decreases the density between 380 and 550 km while increasing it between 250 and 360 km. The $\Delta\delta NE_{\rm Ambi\_diff}$ exhibits relatively weak effects, with only small negative contributions above 300 km. In contrast, $\Delta\delta NE_{E\times B}$ dominates the perturbations in the SED throat region, particularly at 50°–60°N, where $E \times B$ transport sustains substantial electron density enhancement.

Overall, the formation of the SED and TOI has a clear altitude dependence. In the topside ionosphere, upward $E \times B$ drifts lift plasma and increase electron density, whereas below the ionospheric F_2 peak, they reduce it. Neutral winds show a similar contrast, producing plasma accumulation at lower altitudes but depletion at higher altitudes.

Empirical drivers often underestimate storm-time electric fields,

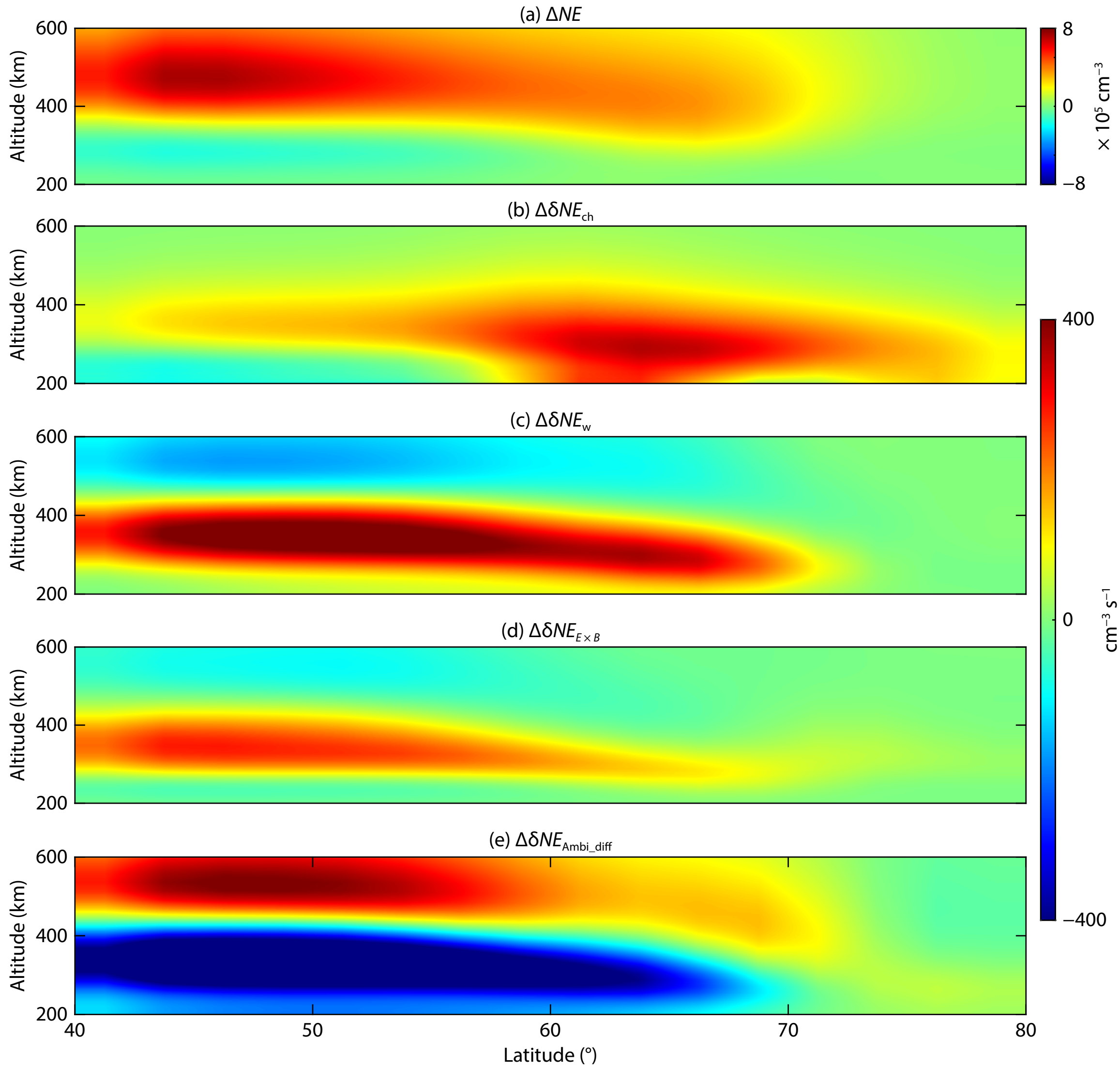

Figure 7. Modeled latitude versus height plots of electron density perturbations and their process-based decomposition from the data-driven TIEGCM simulation on May 10, 2024. The first row shows the total change in electron density (ΔNE, in units of 10^5 cm^{-3}). The following rows show electron density change rates associated with chemical production and loss ($\Delta\delta NE_{\text{ch}}$), neutral wind transport ($\Delta\delta NE_{\text{w}}$), $E \times B$ transport ($\Delta\delta NE_{E\times B}$), and ambipolar diffusion ($\Delta\delta NE_{\text{Ambi\_diff}}$).

smooth out mesoscale structures, and provide only a coarse representation of auroral energy deposition on conductance, often with lower magnitudes and limited spatial detail. As a result, they can only partially capture the vertical structuring of the SED and TOI. In contrast, the data-driven TIEGCM integrates observations through assimilation. SuperDARN-constrained potentials produce stronger, more localized upward $E \times B$ drifts in the dayside throat, persistent topside uplift, and plasma transport into the polar cap. The DMSP SSUSI-constrained auroral energy fluxes enhance nightside auroral deposition, increasing ionization below the ionospheric F_2 peak through electron precipitation and collisions with N_2 and O_2. This process strengthens electron density perturbations in the auroral region. Along the dayside SED channel, enhanced electron density and elevated h_mF_2 reduce molecular recombination and strengthen chemical production, as photoionization remains effective at higher altitudes. Together, these inputs allow the model to capture the distinct processes in the ionosphere and better reproduce the morphology and dynamics of the SED and TOI.

For extreme geomagnetic storms, empirical drivers are often inadequate because their statistical foundations include only a limited number of such events. As a result, they tend to underestimate key high-latitude forcings, such as electric fields and auroral energy deposition, and to excessively smooth the associated spatial structures. In contrast, simulations constrained by observations offer clear advantages by incorporating real-time measurements, enabling dynamic updates and a more faithful representation of mesoscale and small-scale variability under storm-time conditions.

It should also be recognized that tongue-like ionospheric structures can be governed by different dominant mechanisms, depending on the storm phase and latitude. For instance, the middle-latitude daytime tongue-like structure reported during the storm recovery phase was shown to be primarily controlled by the thermospheric composition ($\Sigma O/N_2$; Yu TT et al., 2025). By explicitly distinguishing these different physical regimes, the present study focuses on the electrodynamically organized SED and TOI system during the storm main phase, for which observation-constrained simulations are particularly effective in resolving ionosphere–thermosphere coupling under extreme storm conditions. Future work will benefit from assimilating additional multi-source observations and further improving the representation of coupling processes, thereby enhancing model fidelity and forecasting capability.

5. Summary

This study examines the ionospheric response to the May 10–11, 2024, superstorm by using GNSS TEC observations and TIEGCM simulations. The model is driven by observation-constrained high-latitude inputs: SSUSI auroral energy flux and mean energy assimilated with a multiresolution scheme, together with convection potentials derived from SuperDARN. For comparison, we also perform a controlled experiment using conventional empirical drivers. The main findings are as follows.

We drive the TIEGCM with observation-constrained polar drivers derived through assimilation. At 18:30–20:30 UT on May 10, 2024, SSUSI auroral observations indicate pronounced evening-sector precipitation (16–21 MLT, 60°–70° MLAT) with weaker activity on the dawn side. A multiresolution assimilation of SSUSI retrievals restores mesoscale structure and delivers complete polar coverage, whereas the empirical specification remains overly smooth and too low in amplitude. In addition, incorporating additional data sources into the assimilation would further improve fidelity. Specifically, SuperDARN velocities reveal localized convection, yet its coverage is incomplete. We address this with a SuperDARN-constrained spherical-harmonic solution that retains sharp gradients and fills the gaps. Consequently, the assimilated energy flux, mean energy, and potential fields agree more closely with observations.

From 19:00 to 22:00 UT, storm-time TEC over the American evening–midnight sector intensifies into a plume that extends poleward into the polar cap as a narrow TOI. Overlaying data-driven TEC with convection vectors reveals that the enhancement axis passes through the dayside throat along cross-polar streamlines. A prominent feature is the well-defined two-cell ion convection pattern, and the O/N_2 distribution exhibits a comparable morphology. Under this circulation at 19:00 UT, the combined Δh_mF_2 uplift and ΔN_mF_2 increase delineate the SED source region and the subsequent TOI track. The data-driven TIEGCM more realistically captures TEC amplitudes, the SED plume, and its narrow TOI extension. On the other hand, the TOI structure from the empirical run is broader and smoother, and it underpenetrates the polar cap.

In the topside ionosphere, SuperDARN-constrained potentials yield more dynamic and structurally accurate $E \times B$ drifts that govern plasma uplift and facilitate transport into the polar cap. Neutral winds and downward ambipolar diffusion partially offset the effect of ion drift. Below the ionospheric F_2 peak, assimilating auroral precipitation brings nightside auroral-oval electron densities closer to reality and enriches the mesoscale structure. Meanwhile, neutral winds and photochemical processes primarily determine the spatial extent and intensity of the SED and its polar-cap extension.

Acknowledgments

The Shandong Provincial Natural Science Foundation (Grant No. ZR2022JQ18) supported this work. This work was also supported by the National Natural Science Foundation of China (NNFSC) Youth Program (Grant No. 42304168). J. Zhang was supported by the National Key R&D Program of China (Grant No. 2022YFF0504400) and the NNSFC (Grant Nos. 42188101 and 42174210). We acknowledge the use of data from the Chinese Meridian Project. The construction of the CN-DARN was made possible by funds provided by the Chinese Meridian Project Phase II. The authors acknowledge the use of SuperDARN data and SSUSI data from DMSP satellites. SuperDARN is a network of radars funded by the national scientific funding agencies of Australia, Canada, China, France, Italy, Japan, Norway, South Africa, the United Kingdom, and the United States of America.

Data Availability Statement

The TIEGCM output data used in this paper are accessible upon request (202317798@mail.sdu.edu.cn). The GPS TEC data products can be accessed through the Madrigal distributed data system (http://madrigal.iggcas.ac.cn/). The solar wind parameters were obtained from the OMNI 2 database (https://omniweb.gsfc.nasa.gov/). The auroral mean energy and energy flux data were obtained from the DMSP SSUSI database (https://spdf.gsfc.nasa.gov/pub/data/dmsp/dmspf18/ssusi/data/edr-aurora/).

The SuperDARN potential data can be downloaded from Zhang JJ (2025).

References

Aa, E., Zhang, S. R., Lei, J. H., Huang, F. Q., Erickson, P. J., Coster, A. J., Luo, B. X., and Kerr, R. B. (2024a). Significant midlatitude plasma density peaks and dual-hemisphere SED during the 10–11 May 2024 super geomagnetic storm. *J. Geophys. Res.: Space Phys.*, *129*(11), e2024JA033360. https://doi.org/10.1029/2024JA033360

Aa, E., Dzwill, P., Zhang, S. R., and Erickson, P. J. (2024b). A statistical analysis of the morphology of storm-enhanced density plumes over the North American sector. *J. Geophys. Res.: Space Phys.*, *129*(6), e2024JA032750. https://doi.org/10.1029/2024JA032750

Burns, A. G., Killeen, T. L., Deng, W., Carignan, G. R., and Roble, R. G. (1995). Geomagnetic storm effects in the low- to middle-latitude upper thermosphere. *J. Geophys. Res.: Space Phys.*, *100*(A8), 14673–14691. https://doi.org/10.1029/94ja03232

Burns, A. G., Wang, W., Killeen, T. L., and Solomon, S. C. (2004). A "tongue" of neutral composition. *J. Atmos. Sol.-Terr. Phys.*, *66*(15–16), 1457–1468. https://doi.org/10.1016/j.jastp.2004.04.009

Cherniak, I., Zakharenkova, I., and Redmon, R. J. (2015). Dynamics of the high-latitude ionospheric irregularities during the 17 March 2015 St. Patrick's Day storm: Ground-based GPS measurements. *Space Wea.*, *13*(9), 585–597. https://doi.org/10.1002/2015sw001237

Cherniak, I., and Zakharenkova, I. (2016). High-latitude ionospheric irregularities: Differences between ground- and space-based GPS measurements during the 2015 St. Patrick's Day storm. *Earth, Planets Sp.*, *68*(1), 136. https://doi.org/10.1186/s40623-016-0506-1

Chisham, G., Lester, M., Milan, S. E., Freeman, M. P., Bristow, W. A., Grocott, A., McWilliams, K. A., Ruohoniemi, J. M., Yeoman, T. K., … Walker, A. D. M. (2007). A decade of the Super Dual Auroral Radar Network (SuperDARN): Scientific achievements, new techniques and future directions. *Surv. Geophys.*, *28*(1), 33–109. https://doi.org/10.1007/s10712-007-9017-8

Cousins, E. D. P., and Shepherd, S. G. (2012). Statistical characteristics of small-scale spatial and temporal electric field variability in the high-latitude ionosphere. *J. Geophys. Res.: Space Phys.*, *117*(A3), A03317. https://doi.org/10.1029/2011JA017383

Cousins, E. D. P., Matsuo, T., and Richmond, A. D. (2013). SuperDARN assimilative mapping. *J. Geophys. Res.: Space Phys.*, *118*(12), 7954–7962. https://doi.org/10.1002/2013JA019321

Dang, T., Lei, J. H., Wang, W. B., Wang, B. Y., Zhang, B. Z., Liu, J., Burns, A., and Nishimura, Y. (2019). Formation of double tongues of ionization during the 17 March 2013 geomagnetic storm. *J. Geophys. Res.: Space Phys.*, *124*(12), 10619–10630. https://doi.org/10.1029/2019ja027268

Deng, Y., and Ridley, A. J. (2006), Role of vertical ion convection in the high-latitude ionospheric plasma distribution, *J. Geophys. Res., 111*, A09314, doi:10.1029/2006JA011637.

Du, J. H., and Yang, Z. (2025). Ionospheric response to the May 2024 geomagnetic storm within the SAA region: Analysis with MSS-1, COSMIC-2, and ground-based GNSS data. *Earth Planet. Phys.*, *9*(3), 719–730. https://doi.org/10.26464/epp2025059

Fang, X. H., Randall, C. E., Lummerzheim, D., Solomon, S. C., Mills, M. J., Marsh, D. R., Jackman, C. H., Wang, W. B., and Lu, G. (2008). Electron impact ionization: A new parameterization for 100 eV to 1 MeV electrons. *J. Geophys. Res.: Space Phys.*, *113*(A9), A09311. https://doi.org/10.1029/2008JA013384

Foster, J. C. (1993). Storm time plasma transport at middle and high latitudes. *J. Geophys. Res.: Space Phys.*, *98*(A2), 1675–1689. https://doi.org/10.1029/92ja02032

Foster, J. C., and Rideout, W. (2007). Storm enhanced density: Magnetic conjugacy effects. *Ann. Geophys.*, *25*(8), 1791–1799. https://doi.org/10.5194/angeo-25-1791-2007

Foster, J. C., Rideout, W., Sandel, B., Forrester, W. T., and Rich, F. J. (2007). On the relationship of SAPS to storm-enhanced density. *J. Atmos. Sol.-Terr. Phys.*, *69*(3), 303–313. https://doi.org/10.1016/j.jastp.2006.07.021

Foster, J. C., Zou, S. S., Heelis, R. A., and Erickson, P. J. (2021). Ionospheric storm-enhanced density plumes. In C. S. Huang, et al. (Eds.), *Ionosphere Dynamics and Applications* (pp. 131–151). Washington, DC: American Geophysical Union. https://doi.org/10.1002/9781119815617.ch6

Frey, H. U., Mende, S. B., Angelopoulos, V., and Donovan, E. F. (2004). Substorm onset observations by IMAGE-FUV. *J. Geophys. Res.: Space Phys.*, *109*(A10), A10304. https://doi.org/10.1029/2004JA010607

Hardy, D. A., Gussenhoven, M. S., Raistrick, R., and McNeil, W. J. (1987). Statistical and functional representations of the pattern of auroral energy flux, number flux, and conductivity. *J. Geophys. Res.: Space Phys.*, *92*(A11), 12275–12294. https://doi.org/10.1029/JA092iA11p12275

Heelis, R. A., Lowell, J. K., and Spiro, R. W. (1982). A model of the high-latitude ionospheric convection pattern. *J. Geophys. Res.: Space Phys.*, *87*(A8), 6339–6345. https://doi.org/10.1029/ja087ia08p06339

Heelis, R. A., Sojka, J. J., David, M., and Schunk, R. W. (2009). Storm time density enhancements in the middle-latitude dayside ionosphere. *J. Geophys. Res.: Space Phys.*, *114*(A3), A03315. https://doi.org/10.1029/2008ja013690

Horvath, I., and Lovell, B. C. (2010). Storm-enhanced plasma density features investigated during the Bastille Day Superstorm. *J. Geophys. Res.: Space Phys.*, *115*(A6), A06305. https://doi.org/10.1029/2009ja014674

Huba, J. D., and Drob, D. (2017). SAMI3 prediction of the impact of the 21 August 2017 total solar eclipse on the ionosphere/plasmasphere system. *Geophys. Res. Lett.*, *44*(12), 5928–5935. https://doi.org/10.1002/2017gl073549

Jin, Y. Q., Kotova, D., Clausen, L. B. N., and Miloch, W. J. (2025). Significant plasma density depletion from high- to mid-latitude ionosphere during the super storm in May 2024. *Geophys. Res. Lett.*, *52*(5), e2024GL113997. https://doi.org/10.1029/2024GL113997

Kelley, M. C., Makela, J. J., Chau, J. L., and Nicolls, M. J. (2003). Penetration of the solar wind electric field into the magnetosphere/ionosphere system. *Geophys. Res. Lett.*, *30*(4), 1158. https://doi.org/10.1029/2002gl016321

Kelley, M. C., Vlasov, M. N., Foster, J. C., and Coster, A. J. (2004). A quantitative explanation for the phenomenon known as storm-enhanced density. *Geophys. Res. Lett.*, *31*(19), L19809. https://doi.org/10.1029/2004GL020875

Lei, J. H., Wang, W. B., Burns, A. G., Solomon, S. C., Richmond, A. D., Wiltberger, M., Goncharenko, L. P., Coster, A., and Reinisch, B. W. (2008). Observations and simulations of the ionospheric and thermospheric response to the December 2006 geomagnetic storm: Initial phase. *J. Geophys. Res.: Space Phys.*, *113*(A1), A01314. https://doi.org/10.1029/2007ja012807

Liu, B., Liu, J., Liu, X., Li, S., and Liu, L. (2025). On the relationship between traveling atmospheric disturbances and traveling ionospheric disturbances. *J. Geophys. Res.: Space Phys.*, *130*, e2024JA033271. https://doi.org/10.1029/2024JA033271

Liu, J., Nakamura, T., Liu, L. B., Wang, W. B., Balan, N., Nishiyama, T., Hairston, M. R., and Thomas, E. G. (2015). Formation of polar ionospheric tongue of ionization during minor geomagnetic disturbed conditions. *J. Geophys. Res.: Space Phys.*, *120*(8), 6860–6873. https://doi.org/10.1002/2015ja021393

Liu, J., Wang, W. B., Burns, A., Solomon, S. C., Zhang, S. R., Zhang, Y. L., and Huang, C. S. (2016). Relative importance of horizontal and vertical transports to the formation of ionospheric storm-enhanced density and polar tongue of ionization. *J. Geophys. Res.: Space Phys.*, *121*(8), 8121–8133. https://doi.org/10.1002/2016ja022882

Liu, L. B., and Wan, W. X. (2020). Recent ionospheric investigations in China (2018–2019). *Earth Planet. Phys.*, *4*(3), 179–205. https://doi.org/10.26464/epp2020028

Lu, X., Wu, H. N., Kaeppler, S., Meriwether, J., Nishimura, Y., Wang, W. B., Li, J. T., and Shi, X. L. (2023). Understanding strong neutral vertical winds and ionospheric responses to the 2015 St. Patrick's Day storm using TIEGCM driven by data-assimilated aurora and electric fields. *Space Wea.*, *21*(2), e2022SW003308. https://doi.org/10.1029/2022SW003308

Newell, P. T., Liou, K., Zhang, Y. L., Sotirelis, T. S., Paxton, L. J., and Mitchell, E. J. (2015). Auroral precipitation models and space weather. In Y. L. Zhang, et al. (Eds.), *Auroral Dynamics and Space Weather* (pp. 275–290). Washington, DC: American Geophysical Union. https://doi.org/10.1002/9781118978719.ch18

Nishitani, N., Ruohoniemi, J. M., Lester, M., Baker, J. B. H., Koustov, A. V., Shepherd, S. G., Chisham, G., Hori, T., Thomas, E. G., … Kikuchi, T. (2019). Review of the accomplishments of mid-latitude Super Dual Auroral Radar Network (SuperDARN) HF radars. *Prog. Earth Planet. Sci.*, *6*(1), 27. https://doi.org/10.1186/s40645-019-0270-5

Nychka, D., Bandyopadhyay, S., Hammerling, D., Lindgren, F., and Sain, S. (2015). A multiresolution Gaussian process model for the analysis of large spatial datasets. *J. Comput. Graph. Stat.*, *24*(2), 579–599. https://doi.org/10.1080/10618600.2014.914946

Papitashvili, V. O., and Rich, F. J. (2002). High-latitude ionospheric convection models derived from Defense Meteorological Satellite Program ion drift observations and parameterized by the interplanetary magnetic field strength and direction. *J. Geophys. Res.: Space Phys.*, *107*(A8), 1198. https://doi.org/10.1029/2001ja000264

Paxton, L. J., Meng, C. I., Fountain, G. H., Ogorzalek, B. S., Darlington, E. H., Gary, S. A., Goldsten, J. O., Kusnierkiewicz, D. Y., Lee, S. C., … Smith, B. E. (1992). Special sensor ultraviolet spectrographic imager: An instrument description. In *Proceedings of SPIE 1745, Instrumentation for Planetary and Terrestrial Atmospheric Remote Sensing* (pp. 2–15). San Diego, CA: SPIE. https://doi.org/10.1117/12.60595

Paxton, L. J., and Meng, C. I. (1999). Auroral imaging and space-based optical remote sensing. *Johns Hopkins APL Tech. Dig.*, *20*(4), 556–569.

Pokhotelov, D., Fernandez-Gomez, I., and Borries, C. (2021). Polar tongue of ionisation during geomagnetic superstorm. *Ann. Geophys.*, *39*(5), 833–847. https://doi.org/10.5194/angeo-39-833-2021

Qian, L. Y., Burns, A. G., Emery, B. A., Foster, B., Lu, G., Maute, A., Richmond, A. D., Roble, R. G., Solomon, S. C., and Wang, W. B. (2014). The NCAR TIE-GCM. In J.

Huba, et al. (Eds.), *Modeling the Ionosphere–Thermosphere System* (pp. 73–83). Washington, DC: American Geophysical Union. https://doi.org/10.1002/9781118704417.ch7

Richmond, A. D., Ridley, E. C., and Roble, R. G. (1992). A thermosphere/ionosphere general circulation model with coupled electrodynamics. *Geophys. Res. Lett.*, *19*(6), 601–604. https://doi.org/10.1029/92GL00401

Richmond, A. D., and Thayer, J. P. (2000). Ionospheric electrodynamics: A tutorial. In S. I. Ohtani, et al. (Eds.), *Magnetospheric Current Systems* (pp. 131–175). Washington, DC: American Geophysical Union. https://doi.org/10.1029/GM118p0131

Rishbeth, H., and Garriott, O. K. (1969). *Introduction to Ionospheric Physics*. New York: Academic Press.

Robinson, R. M., Vondrak, R. R., Miller, K., Dabbs, T., and Hardy, D. (1987). On calculating ionospheric conductances from the flux and energy of precipitating electrons. *J. Geophys. Res.: Space Phys.*, *92*(A3), 2565–2569. https://doi.org/10.1029/JA092iA03p02565

Roble, R. G., Ridley, E. C., Richmond, A. D., and Dickinson, R. E. (1988). A coupled thermosphere/ionosphere general circulation model. *Geophys. Res. Lett.*, *15*(12), 1325–1328. https://doi.org/10.1029/GL015i012p01325

Ruohoniemi, J. M., and Greenwald, R. A. (1998). The response of high-latitude convection to a sudden southward IMF turning. *Geophys. Res. Lett.*, *25*, 2913–2916. https://doi.org/10.1029/98GL02212

Shepherd, S. G., and Ruohoniemi, J. M. (2000). Electrostatic potential patterns in the high-latitude ionosphere constrained by SuperDARN measurements. *J. Geophys. Res.: Space Phys.*, *105*(A10), 23005–23014. https://doi.org/10.1029/2000JA000171

Solomon, S. C., Hays, P. B., and Abreu, V. J. (1988). The auroral 6300 Å emission: Observations and modeling. *J. Geophys. Res.: Space Phys.*, *93*(A9), 9867–9882. https://doi.org/10.1029/JA093iA09p09867

Thomas, E. G., Baker, J. B. H., Ruohoniemi, J. M., Clausen, L. B. N., Coster, A. J., Foster, J. C., and Erickson, P. J. (2013). Direct observations of the role of convection electric field in the formation of a polar tongue of ionization from storm enhanced density. *J. Geophys. Res.: Space Phys.*, *118*(3), 1180–1189. https://doi.org/10.1002/jgra.50116

Thomas, E. G., and Shepherd, S. G. (2018). Statistical patterns of ionospheric convection derived from mid-latitude, high-latitude, and Polar SuperDARN HF radar observations. *J. Geophys. Res.: Space Phys.*, *123*(4), 3196–3216. https://doi.org/10.1002/2018JA025280

Torr, M. R., Torr, D. G., Ong, R. A., and Hinteregger, H. E. (1979). Ionization frequencies for major thermospheric constituents as a function of solar cycle 21. *Geophys. Res. Lett.*, *6*(10), 771–774. https://doi.org/10.1029/GL006i010p00771

Tsurutani, B., Mannucci, A., Iijima, B., Abdu, M. A., Sobral, J. H. A., Gonzalez, W., Guarnieri, F., Tsuda, T., Saito, A., … Vasyliunas, V. M. (2004). Global dayside ionospheric uplift and enhancement associated with interplanetary electric fields. *J. Geophys. Res.: Space Phys.*, *109*(A8), A08302. https://doi.org/10.1029/2003JA010342

van der Meeren, C., Oksavik, K., Lorentzen, D., Moen, J. I., and Romano, V. (2014). GPS scintillation and irregularities at the front of an ionization tongue in the nightside polar ionosphere. *J. Geophys. Res.: Space Phys.*, *119*(10), 8624–8636. https://doi.org/10.1002/2014ja020114

Walach, M. T., Grocott, A., Staples, F., and Thomas, E. G. (2022). Super dual auroral radar network expansion and its influence on the derived ionospheric convection pattern. *J. Geophys. Res.: Space Phys.*, *127*(2), e2021JA029559. https://doi.org/10.1029/2021JA029559

Weimer, D. R. (2005). Improved ionospheric electrodynamic models and application to calculating Joule heating rates. *J. Geophys. Res.: Space Phys.*, *110*(A5), A05306. https://doi.org/10.1029/2004JA010884

Wu, H. N., Lu, X., Lu, G., Chu, X. Z., Wang, W. B., Yu, Z. B., Kilcommons, L. M., Knipp, D. J., Wang, B. Y., and Nishimura, Y. (2020). Importance of regional-scale auroral precipitation and electrical field variability to the storm-time thermospheric temperature enhancement and inversion layer (TTEIL) in the Antarctic E region. *J. Geophys. Res.: Space Phys.*, *125*(9), e2020JA028224. https://doi.org/10.1029/2020JA028224

Wu, H. N., and Lu, X. (2022). Data assimilation of high-latitude electric fields: Extension of a multi-resolution Gaussian process model (Lattice Kriging) to vector fields. *Space Wea.*, *20*(1), e2021SW002880. https://doi.org/10.1029/2021SW002880

Wu, H. N., Tan, X. Y., Zhang, Q., Huang, W., Lu, X., Nishimura, Y., and Zhang, Y. L. (2022). Multiresolution data assimilation for auroral energy flux and mean energy using DMSP SSUSI, THEMIS ASI, and an empirical model. *Space Wea.*, *20*(9), e2022SW003146. https://doi.org/10.1029/2022SW003146

Yu, T. T., Ren, Z. P., Zhao, B. Q., Pedatella, N., Wei, Y., Li, S. Y., Zhai, C. Z., and Zhao, L. X. (2025). Coupled thermosphere–ionosphere tongue-like structure during the recovery phase of the geomagnetic storm on 12 May 2021. *J. Geophys. Res.: Space Phys.*, *130*(1), e2024JA033119. https://doi.org/10.1029/2024JA033119

Yuan, Z. G., Deng, X. H., and Wang, J. F. (2008). DMSP/GPS observations of intense ion upflow in the midnight polar ionosphere associated with the SED plume during a super geomagnetic storm. *Geophys. Res. Lett.*, *35*(19), L19110. https://doi.org/10.1029/2008GL035462

Zhang, K. D., Song, H. M., Wang, H., Liu, J., Wang, W. B., Wan, X., Wang, D. D., and Jin, Y. Q. (2023). Dynamics of the tongue of ionizations during the geomagnetic storm on 7 September 2015: The altitudinal dependences. *J. Geophys. Res.: Space Phys.*, *128*(11), e2023JA031735. https://doi.org/10.1029/2023JA031735

Zhang, J. J., Lan, A. L., Yan, J. Y., Deng, X., Wang, W., Li, H., Sun, L. C., Nan, Y., Song, X. C., and Wang, C. (2024). Development of the Chinese dual auroral radar network and preliminary results. *Space Wea.*, *22*(10), e2024SW004131. https://doi.org/10.1029/2024SW004131

Zhang, J. J. (2025). SuperDARN map data for 10 and 11 May 2024 super geomagnetic storm[DS/OL]. V3. Science Data Bank. Retrieved from https://doi.org/10.57760/sciencedb.15777

Zhang, Y., and Paxton, L. J. (2008). An empirical Kp-dependent global auroral model based on TIMED/GUVI FUV data. *J. Atmos. Sol.-Terr. Phys.*, *70*(8–9), 1231–1242. https://doi.org/10.1016/j.jastp.2008.03.008